PHYSICAL REVIEW A VOLUME 40, NUMBER 5 SEPTEMBER 1, 1989

Superelastic scattering of spin-polarized electrons from sodium

J. J. McClelland, M. H. Kelley, and R. J. Celotta
National Institute of Standards and Technology, Gaithersburg, Maryland 20899
(Received 5 May 1989)

Superelastic scattering of spin-polarized electrons from laser-excited sodium atoms has been measured at incident energies of 2.0, 17.9, and 52.3 eV over the angular range 10°–120°. Circularly polarized excitation of the sodium atoms was used to produce pure $3\,^2P_{3/2}$ ($F=3$, $M_F=\pm 3$) states, which are deexcited by collisions with spin-polarized electrons. The spin polarization of both the target electron and the incident electron allows the resolution of triplet and singlet contributions to $L_\perp$, the angular momentum transferred in the collision perpendicular to the scattering plane, and the measurement of r, the ratio of triplet to singlet cross sections. At low energy, agreement with theory is good over the entire angular range for r, but only at small angles for $L_\perp$. At high energy, agreement is excellent over the full angular range.

I. INTRODUCTION

Recently, a great deal of attention has been focused on collisionally induced alignment and orientation of atoms.[1] This type of study is concerned not only with the measurement of cross sections, but also with the determination of the quantum state-to-state transition amplitudes in the target, which describe the collision process at the most fundamental level. Often several degenerate angular momentum states of the target are populated, such as the M_L levels of an $L\neq 0$ state, and the goal is to measure the magnitudes and relative phases of the amplitudes associated with these states. Methods of measurement include superelastic scattering,[2] in which well-defined states are prepared before the collision, or coincidence techniques,[3] in which the quantum state of the target is investigated after the collision by analyzing emitted photons.

The magnitudes and relative phases determined in these experiments are usually parametrized with a set of physical parameters to facilitate interpretation. For example, an $S\rightarrow P$ transition can be described by the three parameters $L_\perp$, $P_{\rm lin}$, and γ. These parameters are simply related to the scattering amplitudes and are conveniently associated with physical concepts: $L_\perp$ is the angular momentum transferred to the atom perpendicular to the scattering plane, $P_{\rm lin}$ is the degree of linear polarization of the atomic charge cloud induced by the collision, and γ is the alignment angle of the charge cloud with respect to the incident electron direction.[4]

A natural extension of electron-collision-induced alignment and orientation studies is the inclusion of the electron-spin parameter in the experiment. The spin states of the incident electron and of the target contribute additional scattering channels to the scattering process. An unpolarized measurement represents an ensemble average over these states, whereas a measurement with polarized collision partners allows their resolution. The result is the ability to make a complete measurement of amplitudes and phases at the most fundamental level.

The orientations of the incident electron and target spins can have an effect on the scattering amplitudes either through the spin-orbit interaction or through exchange.[5] For alignment and orientation studies involving inelastic transitions in low-Z atoms at low impact energies, spin-orbit interactions are usually negligible. Exchange, on the other hand, can be quite significant in these systems. In this case, to see an effect, the electron and target must both be spin polarized before scattering or spin analyzed after scattering. The relative orientations of their spins determine the spin channel in which the scattering takes place. For example, in a "one-electron" target such as sodium, if the target and incident electron are spin polarized parallel to each other, the scattering takes place in a pure triplet state. If they are antiparallel, the scattering is in a superposition of singlet and triplet states. The exchange interaction causes the triplet and singlet channels to have different scattering amplitudes, and hence causes a difference between parallel and antiparallel scattering.

In this paper we present measurements of spin-dependent orientation parameters determined by superelastic scattering of spin-polarized electrons from sodium in the $3P$ state. The framework for analysis of alignment and orientation when spin is resolved has been discussed in detail for the case of sodium $3S\rightarrow 3P$ excitation or deexcitation (superelastic scattering).[6] This relatively straightforward extension of the unpolarized analysis leads to the separation of the quantities $L_\perp$, $P_{\rm lin}$, and γ into singlet and triplet versions, and the addition of a new parameter r, the ratio of triplet to singlet cross sections (averaged over M_L). The new parameters have essentially the same physical interpretation as their unpolarized counterparts; they indicate in addition, however, the characteristics of the target charge cloud when the excitation occurs via the triplet or singlet channel. The current measurements include determinations of $L_\perp$, $L_\perp^S$, $L_\perp^T$, and r at incident electron energies of 2, 17.9, and 52.3 eV ($L_\perp$ is a spin-averaged quantity; the superscripts S and T indicate singlet and triplet, respectively).

For convenience, the relations between these parameters and the scattering amplitudes are given in Eqs. (1)–(4). Subscripts of ± 1 indicate scattering amplitudes

for transitions from $M_L = \pm 1$ states:

$$L_\perp = \frac{Q_{+1} - Q_{-1}}{Q_{+1} + Q_{-1}} , \tag{1}$$

where $Q_{+1} = 3|F^T_{+1}|^2 + |F^S_{+1}|^2$ and $Q_{-1} = 3|F^T_{-1}|^2 + |F^S_{-1}|^2$,

$$r = \frac{|F^T_{+1}|^2 + |F^T_{-1}|^2}{|F^S_{+1}|^2 + |F^S_{-1}|^2} , \tag{2}$$

$$L^T_\perp = \frac{|F^T_{+1}|^2 - |F^T_{-1}|^2}{|F^T_{+1}|^2 + |F^T_{-1}|^2} , \tag{3}$$

$$L^S_\perp = \frac{|F^S_{+1}|^2 - |F^S_{-1}|^2}{|F^S_{+1}|^2 + |F^S_{-1}|^2} . \tag{4}$$

The scattering amplitudes in Eqs. (1)–(4) are expressed in a coordinate system with quantization axis perpendicular to the scattering plane, i.e., the "natural" frame.[7] They are related to the amplitudes in the collision frame (quantization axis along incident electron direction) by

$$F_{\pm 1} = \mp \frac{1}{\sqrt{2}} F^{\text{coll}}_0 - i F^{\text{coll}}_1 . \tag{5}$$

II. DESCRIPTION OF THE EXPERIMENT

The present experimental results were obtained by scattering spin-polarized electrons from optically pumped sodium atoms (see Fig. 1). Initial results have been presented elsewhere.[8–10] Electrons with polarization (26–28 %) perpendicular to the scattering plane are incident on sodium atoms pumped by circularly polarized laser light tuned to the $3S_{1/2}(F=2) \rightarrow 3P_{3/2}(F=3)$ transition. The laser is incident perpendicular to the scattering plane. Electrons scatter from laser excited atoms, causing deexcitation of the atoms and thereby gaining energy in the collision. This process, referred to as superelastic scattering, corresponds to the time inverse of the inelastic process, in which an electron excites the atom from the ground state to the $3P$ state and loses energy. Superelastic and inelastic scattering are thus described by exactly the same scattering amplitudes (or, more precisely, complex conjugate amplitudes), and the same information is obtained by studying either process.

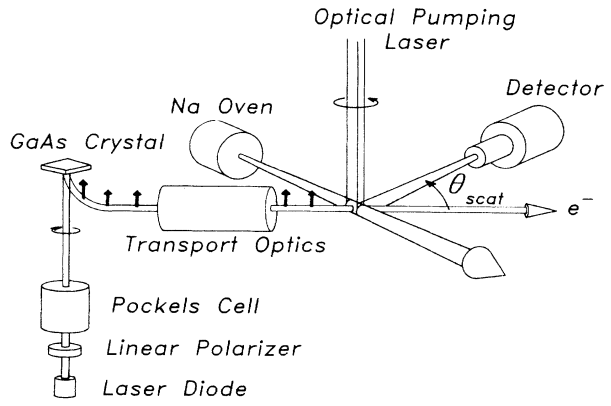

FIG. 1. Schematic of the scattering geometry.

Optical pumping with circularly polarized σ^+ light produces a population of excited sodium atoms in only the $3P_{3/2}(F=3, M_F=+3)$ state (or $M_F=-3$ state for σ^- light).[2] These levels are defined with the quantization axis along the direction of light propagation. The $M_F=+3$ state is a pure angular momentum state of the sodium $3P$ level. It consists of a combination of a pure $M_L=+1$ state, a pure $M_S=+\frac{1}{2}$, state, and a pure $M_I=+\frac{3}{2}$ state (the same holds true for the $M_F=-3$ state, with negative values for M_L, M_S, and M_I). The nuclear-spin quantum number M_I is ignored for the current experiments because the time scale for precession of the atomic angular momenta about the nuclear spin is very long compared to the collision time (Percival-Seaton hypothesis).[11] The pure $M_S=+\frac{1}{2}$ state is a spin-polarized atomic state with spin oriented perpendicular to the scattering plane. The pure $M_L=+1$ state is a fully oriented electronic state of the atom, which allows the measurement of only the $M_L=+1$ scattering amplitude.

Thus, by optically pumping the sodium atoms with σ^+ and σ^- light, and by scattering with electrons polarized "up" and "down" with respect to the scattering plane, we can measure parallel and antiparallel scattering intensities for $M_L=+1$ and -1. We denote the four intensities measured by $I_{R\uparrow}$, $I_{R\downarrow}$, $I_{L\uparrow}$, and $I_{L\downarrow}$, where L and R refer to σ^+ and σ^- (left-handed and right-handed circular polarization), and $\uparrow$ and $\downarrow$ indicate the incident electron-spin orientation. It should be noted that, since our laser is incident from above the scattering plane, the light we refer to as "right-handed" with the subscript R produces atoms that are oriented "up" in the laboratory. As described in Ref. 6, the quantities $L_\perp$, $L^S_\perp$, $L^T_\perp$, and r can be obtained from these intensities as follows. The unpolarized quantity $L_\perp$ is obtained by averaging over the incident electron spin:

$$L_\perp = \frac{(I_{R\uparrow} + I_{R\downarrow}) - (I_{L\uparrow} + I_{L\downarrow})}{(I_{R\uparrow} + I_{R\downarrow}) + (I_{L\uparrow} + I_{L\downarrow})} . \tag{6}$$

The spin-dependent quantities are more conveniently expressed in terms of the measured intensities by first defining "pseudointensities," which correct for the incomplete electron-spin polarization:

$$T_{11} = (1+P_e) I_{R\uparrow} - (1-P_e) I_{R\downarrow} , \tag{7}$$

$$T_{-1-1} = (1+P_e) I_{L\downarrow} - (1-P_e) I_{L\uparrow} , \tag{8}$$

$$S_{11} = (3+P_e) I_{R\downarrow} - (3-P_e) I_{R\uparrow} , \tag{9}$$

$$S_{-1-1} = (3+P_e) I_{L\uparrow} - (3-P_e) I_{L\downarrow} , \tag{10}$$

where P_e is the polarization of the incident electron beam. We then can write

$$L^T_\perp = \frac{T_{11} - T_{-1-1}}{T_{11} + T_{-1-1}} , \tag{11}$$

$$L^S_\perp = \frac{S_{11} - S_{-1-1}}{S_{11} + S_{-1-1}} , \tag{12}$$

$$r=\frac{T_{11}+T_{-1-1}}{S_{11}+S_{-1-1}} . \quad (13)$$

III. APPARATUS

The apparatus used to conduct the experiments described in this paper is shown in Fig. 2. It consists of five main components: a GaAs polarized electron source, a UHV scattering chamber, a sodium oven, a single-frequency stabilized ring-dye laser for optical pumping, and a 100-keV cylindrical Mott analyzer for measuring the polarization of the incident electron beam. These five components will be discussed in the following subsections.

A. GaAs polarized electron source

The principle of the GaAs polarized-electron source used in this work has been described in detail in a previous publication.[12] Polarized electrons are produced by photoemission from a Cs- and O_2-coated GaAs crystal. The photoemission light is obtained from a GaAlAs laser diode operating at 810 nm. The laser light is circularly polarized by passing it through a linear polarizer and a Pockels cell, the Pockels cell being energized with its appropriate quarter-wave voltage. When photoemission is produced with circularly polarized light, the emitted electrons have a net spin polarization because of the magnetic sublevel configuration of the GaAs band structure. This polarization is generally about 28% at room temperature, depending on the particular crystal in use.

On the apparatus, the GaAs crystal is oriented horizontally and the laser diode beam is incident from below. The electrons are thus photoemitted in a downward direction in the laboratory, with spin polarization either up or down, depending on the handedness of the circular polarization of the laser light, which is determined by the polarity of the Pockels-cell voltage. After leaving the photocathode, the electrons enter a quarter-sphere electrostatic deflector which bends the electron beam by 90°. Since the electron spin is not affected by the electric field of the deflector, a horizontal beam with transverse polarization, up or down in the laboratory, is produced. The electron beam is accelerated to 1000 V for transport through an isolation valve, and then passes through a series of optics which produce a beam of energy between 2 and 100 eV focused at the scattering center with a nominal spot size of 2 mm and a divergence half-angle of 35 mrad. The beam current ranges from a few tenths of a μA at 2 eV, to several μA at the higher energies. The energy width of the electron beam is about 0.1 eV.

The electron optics leading to the 1000-V transport region are described in Ref. 12. The deceleration optics are designed so that the focal properties remain essentially constant as the beam energy is varied. All lens elements, with the exception of the last two elements, have fixed voltages with respect to the cathode, which is biased negative (with respect to ground) at the desired beam voltage. The next-to-last element has a positive voltage with respect to ground, maintained at four times the cathode bias voltage. The last element is at ground potential, which is the same as the scattering region. Thus, when the electron energy is scanned by varying the cathode bias, the only other voltage that needs to be changed is the one on the next-to-last lens element. This is done with a power supply linearly programmed by the cathode bias power supply. All lens elements are fabricated from oxygen-free high-conductivity copper, with the exception of the last three elements, which are made from molybdenum to provide a more stable work function surface for the low energy electrons. Magnetic shielding is provided along the length of the optics by a μ-metal lining on the inside of the vacuum wall.

B. Scattering chamber

The scattering chamber is of standard ultra-high-vacuum construction, fabricated from 304 stainless steel.

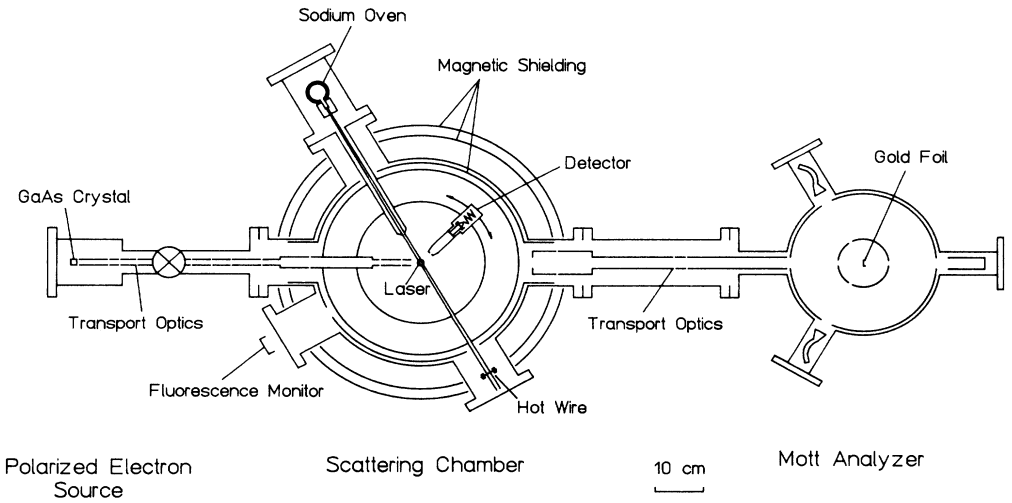

FIG. 2. Polarized-electron–polarized-atom scattering apparatus, showing GaAs polarized-electron source, scattering chamber, sodium oven, and Mott spin analyzer.

A 270-l/s ion pump produces a base pressure of 2×10^{-10} Torr. The chamber is fitted with triple μ-metal shielding, one shield inside and two outside, which reduces the residual magnetic field in the scattering region to less than 0.4 mG. The scattering region is electrostatically shielded by a molybdenum mesh held at the same potential as the last lens element of the transport optics and the entrance of the detector.

The detector, mounted on a turntable, consists of a pair of entrance apertures, an einzel lens retarding field analyzer, and a channel electron multiplier. The resolution of the retarding field analyzer is about 1 eV. In typical operation, the retarding element is held at a potential ~1.1 V more negative than the cathode. The resolution of the analyzer is sufficient to reject effectively the electrons that are elastically and inelastically scattered, and also background electrons, while allowing the 2.1 eV more energetic superelastically scattered electrons to reach the multiplier. The channel electron multiplier cone is held at $+200$ V.

The first aperture on the detector is 6.5 mm in diameter and 25 mm from the scattering center, and the second is 3 mm in diameter and 86 mm from the scattering center. With this arrangement, the detector's field of view at the scattering center is 8 mm in diameter, which is nominally the largest dimension of the cylindrical overlap of the electron beam and the atom beam. The angular resolution of this aperture configuration is $\pm3\frac{1}{2}°$.

C. Sodium oven

The sodium oven, shown in Fig. 3, is contained in a differentially pumped vacuum chamber mounted on the side of the main chamber. A pressure of a few times 10^{-9} Torr is typical during operation of the oven. The sodium beam crosses the scattering center in the scattering plane at an angle of 120° with respect to the incident electron beam. A sodium reservoir, capable of holding about 20 g of sodium, is maintained at about 400–420 °C. The nozzle, with a 1-mm exit hole, is mounted above the reservoir. It is kept at about 500 °C to avoid clogging and to ensure dissociation of sodium dimers. Surrounding the nozzle is a recirculator chamber with a 3.2-mm exit hole. This chamber is held at about 150 °C, at which temperature sodium condenses to a relatively free-flowing liquid. Excess sodium emitted from the nozzle strikes this recirculator, condenses on it, and flows down to the bottom, where a 6.3-mm-diam tube carries the sodium back to the reservoir. Recirculation of sodium in this manner results in very efficient use of a sodium charge. Under normal circumstances, a single filling of the oven provides several hundred hours of operation.

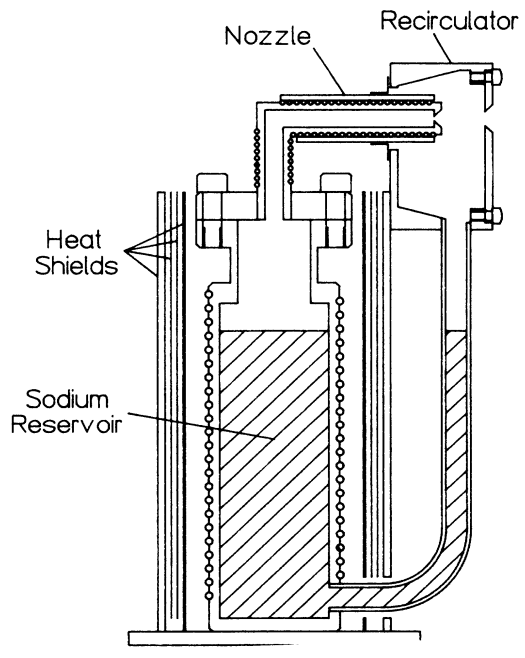

FIG. 3. Recirculating sodium oven. Typical operating temperatures are as follows: sodium reservoir, 410 °C; nozzle, 500 °C; and recirculator, 150 °C.

The sodium beam is collimated by a 3.2-mm aperture located 60 mm from the scattering center. The distance from the nozzle aperture to the collimation aperture is 316 mm, giving the atomic beam a divergence half-angle of 5 mrad. The atom beam is about 4 mm in diameter at the scattering center. The atomic density is about 5×10^{9} atoms/cm^3 under normal operating conditions. Sodium beam flux is monitored by an rhenium hot-wire detector mounted on the far side of the scattering chamber.

D. Optical pumping

Some of the details of the optical pumping methods used have been given in a previous publication.[13] A stabilized, single-frequency ring-dye laser, pumped by 6 W of 514.5 nm light from an argon-ion laser, produces about 600 mW of light tuned to the 589.0-nm $3^2S_{1/2}(F=2)\rightarrow3\,^2P_{3/2}(F=3)$ hyperfine transition in sodium. The laser beam passes through a rotatable half-wave plate and linear polarizer (these act as a variable attenuator), is transported from the laser table to the top of the scattering chamber, passes through a circular polarizer, and enters the chamber from above through a 10-cm vacuum window. The circular polarizer consists of a Glan-Thompson linear polarizer followed by a zeroth-order quarter-wave plate mounted in a rotatable housing. The zeroth-order quarter-wave plate is constructed from two many-order plates mounted on either end of a 1-cm aluminum tube. It was found that this configuration was less sensitive to temperature effects than a zeroth-order plate made from two many-order plates optically in contact with each other. The rotatable housing rotates freely between two stops separated by precisely 90°. Rotation is done with an air-actuated lever under computer control. Right-handed or left-handed circularly polarized light with polarization better than 99.98% is generated reproducibly with this arrangement. Tests for birefringence in the vacuum window were done, and it was found that the effect on the polarization was a few parts in 10^4. The laser beam at the scattering volume is estimated to have about 100 mW of power and has a diameter of about 1 cm ($1/e^2$).

E. Mott analyzer

The polarization of the electron beam is determined with a 100-keV cylindrical Mott analyzer mounted on the scattering chamber directly opposite the electron source. The two chambers are connected by transport optics, in which the polarized electron beam is accelerated to a nominal energy of 1000 V to minimize depolarization by stray fields.

The Mott spin analyzer, based on a design by Hodge *et al.*,[14] consists of two concentric cylinders with axes oriented perpendicular to the electron beam along the direction of the spin to be measured (i.e., vertical in our apparatus). The outer cylinder is held near ground potential, and the inner cylinder is maintained at $+100$ kV. At the center of the inner cylinder is a gold foil. Two detectors are mounted at $\pm 120°$ with respect to the incident electron beam.

The polarized electron beam enters the Mott analyzer through an aperture in the outer cylinder, is accelerated to 100 keV as it passes through an aperture in the inner cylinder, and scatters from the gold foil. Polarized electrons scatter preferentially to one side or the other depending on the orientation of their spin. The left-right asymmetry of the two detector signals thus provides a measure of the polarization of the electrons. To obtain an absolute measure, the "resolving power," or effective Sherman function, of gold at 100 keV and 120° must be known.

A more detailed discussion of how our polarization is measured is found in a recent publication.[15] Measurements performed during the experiments presented in this paper gave $26.0 \pm 1.6\,\%$ for the 2.0-eV results. For the higher-energy measurements, which were conducted with a different GaAs crystal in the source, the polarization was $28.0 \pm 1.7\,\%$.

F. Electron-beam-energy calibration

The energy of the electron beam was calibrated by measuring the onset of electron-impact ionization of sodium at 5.14 eV. The electron detector was rotated to a position close to the sodium beam and biased to detect positive ions. The front of the detector and the retarding element were biased at about -0.5 to -1.0 V with respect to the scattering region, and the cone of the channel electron multiplier was biased at -1000 V (tests were done at different biases on the front of the detector to ensure that this voltage was not affecting the beam energy). Na^+ ions were detected as a function of electron-beam energy over the range 4–6 eV. The ionization probability increases approximately linearly from threshold up to about 6 eV. Linear extrapolation of the measured ionization was done to determine the intercept with the energy axis. This intercept was taken to be at an energy of 5.14 eV. The precision of this method is estimated to be roughly ± 0.1 eV.

Since the work functions are very different for the cathode material (GaAs with Cs and O_2) and the scattering chamber material (molybdenum), the cathode bias voltage necessary to produce a 5.14-eV beam is quite different from 5.14 V. This voltage difference, typically about 3.76 V, is provided by an additional small power supply in series with the cathode bias supply. The additional supply was adjusted so that an electron beam of 5.14 eV kinetic energy was obtained when the cathode bias supply read 5.14 V. This was done so that the electron-beam energy could be set by adjusting the cathode power supply directly, and also so that the voltage on the next-to-last lens element could be programmed directly from the cathode bias supply.

IV. EXPERIMENTAL PROTOCOL

The data shown here were collected using a double modulation technique, in which the polarizations of the electron beam and the atomic beam are switched quickly, while a running average of counts is accumulated over a long period of time. The electron-beam polarization was modulated at 100 Hz by applying a high-voltage square wave to the Pockels cell, and the atom-beam optical pumping laser polarization was flipped from right-handed to left-handed at intervals ranging from 1 to 10 s. Pulses from the channel electron multiplier were routed to one of two scalers, depending on the phase of the Pockels-cell modulation, and these scalars were read each time the optical pumping laser polarization was switched. In addition, after both optical pumping polarizations were measured, the laser was blocked with a shutter and a background was measured. A single measurement of each atomic polarization and background constituted a single measurement cycle. Many cycles were accumulated for each run, which lasted typically $\frac{1}{2}$–1 h. Several runs were carried out at each energy and angle and the results were averaged.

In all, four count rates were measured for each cycle, corresponding to the four combinations of electron-spin orientation and optical pumping polarization. Additionally, the background signals for spin-up and spin-down incident electrons were collected separately in each cycle. The spin dependence of the background was checked on numerous occasions and was always found to be negligible. Therefore, the two backgrounds were averaged, and the average was subtracted from each of the four signals at the end of each cycle.

Count rates varied from a few hundred c/s to less than 1 c/s, depending on scattering angle, energy, and handedness of the optical pumping laser. The background was, at worst, 50% of the total signal, at the smaller angles, but was generally 10% or less at the larger angles. Measurements at positive angles from 10°–70° and at negative angles from 10°–40° and 80°–120° were performed (gaps in the angular coverage were a result of the sodium beam's position in the scattering plane). Where the positive and negative angular ranges overlapped, results were compared invoking basic symmetry considerations, e.g., scattering to the left with spin up from $M_L = +1$ atoms should be the same as scattering to the right with spin down from $M_L = -1$ atoms. Agreement was observed in these regions, and the signals were averaged.

All averaging was performed on intensities before any of the quantities in Eqs. (6)–(13) were calculated. The averaging of different runs was preceded by normalizing

each set of four intensities to the $I_{R\uparrow}$ signal (or $I_{L\downarrow}$ for negative angles). This was done in order to put runs made with different electron-beam intensities and atom-beam densities on the same scale.

Experimental errors were dominated by three major sources: counting statistics, uncertainty in the electron beam polarization, and excited-state population fluctuations. Statistical error estimates were obtained for each of the four count rates by taking the square root of the total number of counts collected. These estimates were propagated in the standard way[16] through the subtraction of the background and the averaging. Their contributions to the error estimates for the quantities in Eqs. (6)–(13), along with the contribution of the $\pm 1.6\%$ error in P_e, were calculated as discussed in the Appendix.

The excited-state population fluctuations were due to laser intensity fluctuations and to slight variations in the degree of circular polarization from cycle to cycle. Both these sources have negligible components at the 100-Hz modulation frequency of the electron-beam polarization; the former as measured with a spectrum analyzer, and the latter because the polarizer is not moved during each phase of the cycle. They do, however, have a combined estimated magnitude of about 3% at the frequency of the optical pumping polarizer modulation (1–10-s period). Thus this error source does not contribute to each of the four intensities independently, but rather only to the two pairs of intensities corresponding to the two atomic optical pumping polarizations. The contribution of such errors to the quantities in Eqs. (6)–(13) can be estimated by propagating 3% relative errors, as discussed in the Appendix. This was done, and the result was added in quadrature with the uncertainty estimates obtained from counting statistics and the uncertainty estimate in P_e. The total is displayed in the figures as error bars, which are intended to be interpreted as one standard deviation.

V. RESULTS AND DISCUSSION

Figure 4 shows the results for 2.0 eV incident electron energy. This corresponds to 4.1 eV incident energy in the equivalent inelastic process. The unpolarized $L_\perp$ is shown in Fig. 4(a), along with the superelastic experimental results of Hermann *et al.*[17] at 3 eV incident energy. These unpolarized data were presented in a previous publication,[10] and are included here for the sake of comparison. Also shown, with a solid line, are the four-state close-coupling theoretical results of Moores and Norcross[18] at an inelastic energy of 4.0 eV, corresponding to a 1.9-eV superelastic energy. At small angles, the theory and the two experiments are in agreement. At larger angles, however, beyond about 40°, a marked discrepancy is evident, with the difference between experiment and theory surpassing a factor of 2 at 120°. This discrepancy at large angles is surprising at this low an incident energy, where close-coupling methods should be reasonably accurate. The energy is below the ionization threshold, so loss of flux to continuum channels does not present a significant complicating factor in the theory. Possible explanations for the discrepancy include core polarization effects, or, conceivably, partial-wave convergence difficulties. It is also possible, though rather unlikely, that the energy difference of 0.1 eV between experiment and theory could be the cause of the discrepancy, if resonancelike behavior is causing rapid variations in $L_\perp$ as a function of energy. Such sharp energy dependence in $L_\perp$ has not been investigated in theory or experiment, so it cannot be completely ruled out. Resonances in the total cross section for sodium, however, are quite small in this energy region.[19]

Further insight into the discrepancy between experiment and theory can be obtained by examining the quantities $L_\perp^S$ and $L_\perp^T$, shown in Fig. 4(b), where the data points show the current measurement and the lines show the calculations of Moores and Norcross.[18] Here we see that at small angles, the two channels have relatively

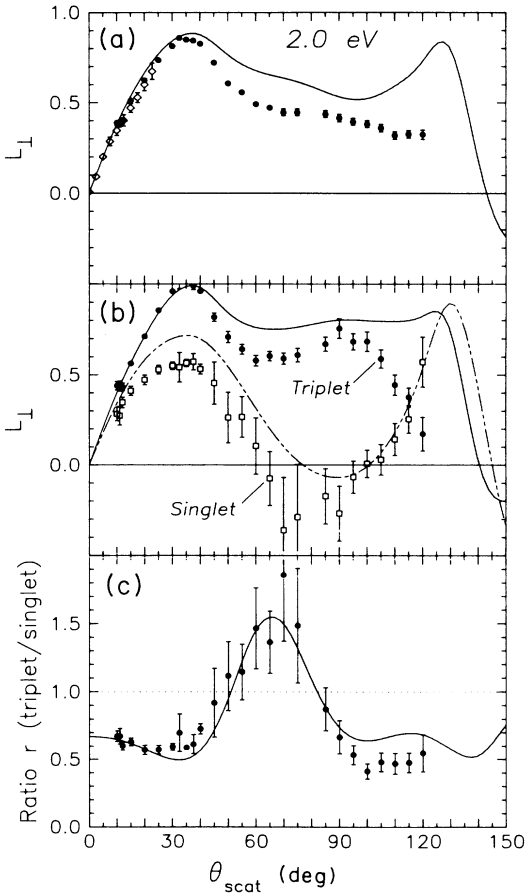

FIG. 4. Spin-polarized superelastic scattering from Na($3P$) at 2 eV incident energy vs scattering angle θ_{scat}. (a) Unpolarized measurement of angular momentum transferred perpendicular to the scattering plane $L_\perp$. Solid circles, present work; open diamonds, experiment of Hermann *et al.* (Ref. 17) (3 eV incident energy); solid line, four-state close-coupling calculation of Moores and Norcross (Ref. 18). (b) Singlet (open squares) and triplet (solid circles) perpendicular angular momentum transfer $L_\perp^S$ and $L_\perp^T$, with calculations of Moores and Norcross (Ref. 18) (solid and dashed curves). (c) Ratio r of triplet to singlet cross sections. Solid circles, present work; solid line, theory of Moores and Norcross (Ref. 18).

similar behavior. The singlet value of $L_\perp$ is lower than the triplet value, but both show the characteristic sharp increase from near zero at small scattering angles. At the smallest angles, reasonable agreement between theory and experiment is observed in both channels. After about 20°, however, the singlet channel begins to differ from theory while the triplet channel continues to agree. At intermediate angles, where the unpolarized $L_\perp$ measurements begin to differ from the theory, we see that $L_\perp^S$ and $L_\perp^T$ begin to take on widely differing values. The singlet version goes briefly negative, while the triplet version stays closer to the unpolarized value. The agreement with theory is somewhat worse in this region, and seems to be equally shared between the two channels. Beyond about 90°, in the region where a severe discrepancy between theory and experiment is observed in the unpolarized data, we see that, in contrast with small angles, it is the singlet $L_\perp$ that shows good agreement with the theory, while the triplet value begins to deviate strongly.

Figure 4(c) shows the ratio r of triplet-to-singlet cross sections. It is less than 1 at small and large angles, indicating a smaller triplet cross section, and larger than 1 at intermediate angles, indicating that the singlet channel has a smaller cross section in this region. The agreement with the close-coupling calculation is excellent across the entire angular range. This is encouraging, because the calculation uses a fully antisymmetrized wave function for the target and scattered electron as a system, and hence should treat exchange rigorously.

By examining the measurements of $L_\perp^S$, $L_\perp^T$, and r, we can draw some conclusions about the relationship between theory and experiment in the unpolarized $L_\perp$ measurement. By comparing Figs. 4(a) and 4(b), we see that the behavior of the unpolarized $L_\perp$ appears to be dominated by the triplet channel over most of the angular range. Both $L_\perp$ and $L_\perp^T$ agree well with the theory at small angles, but disagree at large angles. This can be understood in terms of the ratio r when one takes into account the fact that the triplet channel has a threefold degeneracy, and hence carries three times the weight of the singlet channel. Even though r indicates that the singlet cross section is larger than the triplet at small and large angles, it is not large enough to overcome the weighting factor. The ratio r would have to fall below 0.33 before the singlet $L_\perp$ would begin to dominate.

This type of comparison with theory shows that a great deal more information can be obtained by separating singlet and triplet channels in a spin-polarized experiment. Not only are we are able to narrow down the source of discrepancy between theory and experiment to a particular spin channel, but we also obtain three times the amount of information from the experiment, providing unprecedented detail for comparison with theory.

In Fig. 5, we show measurements of $L_\perp$, $L_\perp^S$, $L_\perp^T$, and r at an incident electron energy of 17.9 eV. This energy corresponds to an inelastic incident energy of 20 eV. The behavior of $L_\perp$ at this energy, shown in Fig. 5(a), is more complex than at 2.0 eV. It shows two positive peaks in the forward direction, then rapidly becomes negative, crossing zero at $\sim 60°$ and reaching a value of almost -1.0 at 70°. The negative peak is followed by an increase

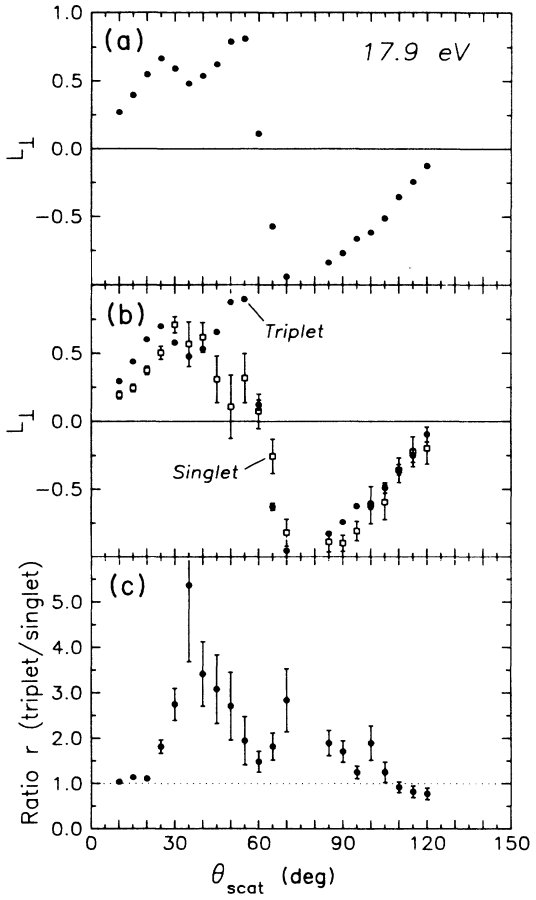

FIG. 5. Spin-polarized superelastic scattering from Na(3P) at 17.9 eV incident energy vs scattering angle θ_{scat}. (a) Unpolarized measurement of angular momentum transferred perpendicular to the scattering plane $L_\perp$. (b) Singlet (open squares) and triplet (solid circles) perpendicular angular momentum transfer $L_\perp^S$ and $L_\perp^T$. (c) Ratio r of triplet to singlet cross sections.

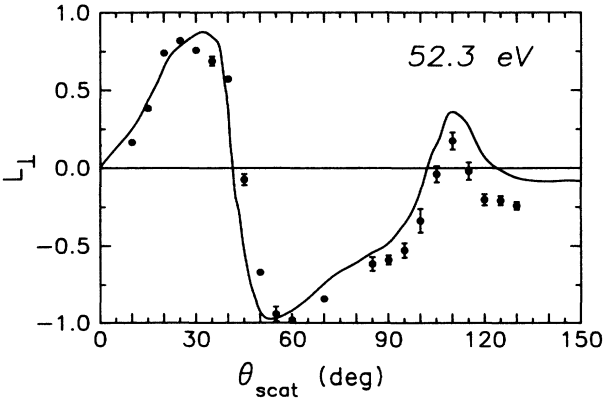

FIG. 6. Superelastic scattering from Na(3P) at 52.3 eV incident energy vs scattering angle θ_{scat}. Unpolarized measurement of angular momentum transferred perpendicular to the scattering plane $L_\perp$. Solid circles, present work; solid line, four-state close-coupling calculation of Mitroy *et al.* (Ref. 20).

toward zero over the range 70°–120°.

The separation of $L_\perp$ into singlet and triplet channels is shown in Fig. 5(b). The difference between $L_\perp^S$ and $L_\perp^T$ is not as dramatic as it is at 2.0 eV, as might be expected, because at the higher energy, exchange should play a lesser role. Nevertheless, some differences still exist, most notably in the region of the double peaks at 45° and 55°. Both singlet and triplet channels have roughly the same first peak, but the second peak appears to arise only from the triplet channel. At large angles, where one might expect exchange to be more significant, the singlet and triplet channels have almost identical values of $L_\perp$.

The ratio r of singlet-to-triplet cross sections, shown in Fig. 5(c), has angular dependence qualitatively similar to the 2.0-eV ratio, though it has two apparent peaks at $\sim 40°$ and $\sim 75°$ and never gets very far below a value of 1.0. The triplet cross sections seems to be dominant across most of the angular range at this energy. Interestingly, though $L_\perp$ shows less difference between singlet and triplet at the higher energy, r is in fact larger at the higher energy. That r is larger at higher energy shows that simple arguments about the energy dependence of exchange are dangerous at these low energies. That $L_\perp$ and r do not exhibit the same sensitivity to exchange can be explained by noting that these two parameters provide very different measures of exchange, and are quite independent of each other [see Eqs. (1)–(4)].

At present, there are not calculations available in the literature at this energy suitable for comparison with these data. It is hoped that these measurements will stimulate further work on this subject.

Figure 6 contains measurements of $L_\perp$ at an incident energy of 52.3 eV. This energy was chosen to match an existing inelastic calculation at 54.4 eV (4 Ry). The behavior of $L_\perp$ at this high energy is qualitatively similar to the behavior at 17.9 eV, though the curve seems to be compressed to smaller angles. This is consistent with a simple kinematic picture of equal momentum transfer in small-angle scattering at a high energy and large-angle scattering at a low energy. The double peak at small angles is absent, but the general trend of a large positive peak followed by a sharp drop to nearly -1.0 is evident. The higher-energy curve has the additional feature of a small positive peak at the largest angles. The determinations of $L_\perp^S$, $L_\perp^T$, and r were also carried out at this energy, but statistical errors were so large that we could see no difference between $L_\perp^S$ and $L_\perp^T$, nor did r deviate from a value of 1. This is consistent with the notion that at this high an energy, exchange should really be a small effect, but our experimental results are not able to support this with any strength.

The solid curve shown in Fig. 6 is the four-state close-coupling calculation of Mitroy *et al.*[20] Agreement between experiment and theory is excellent across the entire angular range. This is especially remarkable, considering the rich structure of the curve, indicating complex interference effects between many partial waves.

VI. CONCLUSIONS

We have presented measurements of spin-dependent orientation parameters for the Na $3S \rightarrow 3P$ transition. This represents a significant step in the progression toward a complete measurement of all the amplitudes and relative phases which describe the transition. If one includes a measurement of the differential cross section, which can be done by conventional electron-scattering techniques, four of the seven necessary quantities are measured. These four quantities, the cross section σ_0, $L_\perp^S$, $L_\perp^T$, and r, relate directly to the magnitudes of the four scattering amplitudes F_{+1}^S, F_{-1}^S, F_{+1}^T, and F_{-1}^T. The only remaining quantities to be measured are the relative phases between these amplitudes. Some information has already been obtained on this from measurements of $P_{\rm lin}$ with unpolarized electrons,[1] but the phase between singlet and triplet amplitudes must be obtained with spin-polarized measurements.

Comparisons with theory have been presented, and some interesting discrepancies and agreements have been found. It is hoped that these comparisons will stimulate further work on the theoretical front. The amount of detail available with this type of experiment should provide an excellent basis for critical comparison with new theoretical approaches, and should provide insight into where problems, if any exist, are located in the calculations.

Future work is planned to be directed toward, among other things, the complete determination of all amplitudes and relative phases. This can be accomplished by analyzing the spin of the scattered electron in addition to using polarized incident electrons and atoms, or by using more exotic optical pumping polarizations and angles of incidence (see Ref. 6). In addition, work on other transitions in sodium, and on other atoms, is planned to expand this new body of information in electron-atom scattering.

ACKNOWLEDGMENTS

The authors wish to thank S. R. Mielczarek, W. T. Rogers, and B. J. Waclawski for experimental support in the early stages of this work. We also wish to thank D. H. Oza for valuable theoretical discussions. This work is supported in part by the U.S. Department of Energy, Office of Energy Research, Division of Chemical Sciences.

APPENDIX

In this appendix we present expressions for the uncertainties of the quantities in Eqs. (6)–(13) in terms of the uncertainties in the intensities and electron-beam polarization. These expressions are derived in the standard manner,[16] assuming the intensity errors are uncorrelated.

Any quantity A, which is a function of several parameters x_i having uncorrelated uncertainties δx_i, has an uncertainty δA given by

$$(\delta A)^2 = \sum_i \left[\frac{\partial A}{\partial x_i} \right]^2 (\delta x_i)^2 \ . \tag{A1}$$

Applying this result to Eqs. (6)–(13), which give the quantities of interest in terms of the intensities, we obtain the following uncertainties:

$$(\delta L_\perp)^2=(I_{\rm tot})^{-2}[(1-L_\perp)^2(\delta I_{R\uparrow})^2+(1-L_\perp)^2(\delta I_{R\downarrow})^2+(1+L_\perp)^2(\delta I_{L\uparrow})^2+(1+L_\perp)^2(\delta I_{L\downarrow})^2]\ , \tag{A2}$$

$$(\delta L_\perp^S)^2=(I_{\rm tot}^S)^{-2}[(I_R-I_L-L_\perp^S I_R-L_\perp^S I_L)^2(\delta P_e)^2+(1-L_\perp^S)^2(3-P_e)^2(\delta I_{R\uparrow})^2$$
$$+(1-L_\perp^S)^2(3+P_e)^2(\delta I_{R\downarrow})^2+(1+L_\perp^S)^2(3+P_e)^2(\delta I_{L\uparrow})^2+(1+L_\perp^S)^2(3-P_e)^2(\delta I_{L\downarrow})^2]\ , \tag{A3}$$

$$(\delta L_\perp^T)^2=(I_{\rm tot}^T)^{-2}[(I_R-I_L-L_\perp^T I_R-L_\perp^T I_L)^2(\delta P_e)^2+(1-L_\perp^T)^2(1+P_e)^2(\delta I_{R\uparrow})^2$$
$$+(1-L_\perp^T)^2(1-P_e)^2(\delta I_{R\downarrow})^2+(1+L_\perp^T)^2(1-P_e)^2(\delta I_{L\uparrow})^2+(1+L_\perp^T)^2(1+P_e)^2(\delta I_{L\downarrow})^2]\ , \tag{A4}$$

$$(\delta r)^2=(I_{\rm tot}^S)^{-2}[I_{\rm tot}^2(1-r)^2(\delta P_e)^2+(1+P_e+3r-rP_e)^2(\delta I_{R\uparrow})^2+(1-P_e+3r+rP_e)^2(\delta I_{R\downarrow})^2$$
$$+(1-P_e+3r+rP_e)^2(\delta I_{L\uparrow})^2+(1+P_e+3r-rP_e)^2(\delta I_{L\downarrow})^2]\ , \tag{A5}$$

where we have defined, for convenience,

$$I_{\rm tot}=I_{R\uparrow}+I_{R\downarrow}+I_{L\uparrow}+I_{L\downarrow}\ , \tag{A6}$$

$$I_R=I_{R\uparrow}+I_{R\downarrow}\ , \tag{A7}$$

$$I_L=I_{L\uparrow}+I_{L\downarrow}\ , \tag{A8}$$

$$I_{\rm tot}^S=(3+P_e)I_{R\downarrow}-(3-P_e)I_{R\uparrow}+(3+P_e)I_{L\uparrow}$$
$$-(3-P_e)I_{L\downarrow}\ , \tag{A9}$$

$$I_{\rm tot}^T=(1+P_e)I_{R\uparrow}-(1-P_e)I_{R\downarrow}+(1+P_e)I_{L\downarrow}$$
$$-(1-P_e)I_{L\uparrow}\ . \tag{A10}$$

These expressions were used to calculate the statistical error estimates, using $(\delta I_{R\uparrow})^2=I_{R\uparrow}$, $(\delta I_{R\downarrow})^2=I_{R\downarrow}$, $(\delta I_{L\uparrow})^2=I_{L\uparrow}$, $(\delta I_{L\downarrow})^2=I_{L\downarrow}$, and $\delta P_e=0.016$.

The additional uncertainty introduced in the $L_\perp$ measurements by laser intensity and polarization noise can be determined by noting that if the noise is slow compared with the electron spin modulation, it can be modeled as noise in the intensities for right-handed and left-handed polarization only, independent of the electron-spin polarization. This corresponds to noise in I_R and I_L for $L_\perp$, T_{11} and T_{-1-1} for $L_\perp^T$, and S_{11} and S_{-1-1} for $L_\perp^S$. Since $L_\perp$, $L_\perp^S$, and $L_\perp^T$ all have the same algebraic form (i.e., a generic asymmetry), the analysis is the same for all three if we make the correspondences $I_R\leftrightarrow T_{11}\leftrightarrow S_{11}$, $I_L\leftrightarrow T_{-1-1}\leftrightarrow S_{-1-1}$, and $I_{\rm tot}\leftrightarrow I_{\rm tot}^T\leftrightarrow I_{\rm tot}^S$. We will discuss the uncertainty in terms of I_R and I_L with the understanding that the result can be applied equally to all three types of $L_\perp$ using these correspondences. Letting the intensity noise be a constant fraction of the signal, i.e., $\delta I_R=\alpha I_R$, $\delta I_L=\alpha I_L$ we obtain for the additional uncertainty in $L_\perp$

$$(\delta L_\perp)^2=I_{\rm tot}^{-2}\alpha^2[(1-L_\perp)^2I_R^2+(1+L_\perp)^2I_L^2]\ . \tag{A11}$$

As discussed in the text, an estimated α of 0.03 was used in this expression. The resulting $\delta L_\perp$ was added in quadrature to the uncertainty derived from statistical and P_e errors, since these error sources are assumed to be random and uncorrelated.

[1] N. Anderson, J. W. Gallagher, and I. V. Hertel, Phys. Rep. **165**, 1 (1988).

[2] I. V. Hertel and W. Stoll, Adv. Atom. Mol. Phys. **13**, 113 (1977).

[3] M. Eminyan, K. B. MacAdam, J. Slevin, and H. Kleinpoppen, J. Phys. B **7**, 1519 (1974).

[4] N. Anderson and I. V. Hertel, Comm. At. Mol. Phys. **19**, 1 (1986).

[5] J. Kessler, *Polarized Electrons*, 2nd ed. (Springer, Berlin, 1985).

[6] I. V. Hertel, M. H. Kelley, and J. J. McClelland, Z. Phys. D **6**, 163 (1987).

[7] H. W. Hermann and I. V. Hertel, Comm. At. Mol. Phys. **12**, 61 (1982).

[8] J. J. McClelland, M. H. Kelley, and R. J. Celotta, Phys. Rev. Lett. **55**, 688 (1985).

[9] J. J. McClelland, M. H. Kelley, and R. J. Celotta, Phys. Rev. Lett. **56**, 1362 (1986).

[10] J. J. McClelland, M. H. Kelley, and R. J. Celotta, J. Phys. B **20**, L385 (1987).

[11] I. C. Percival and M. J. Seaton, Philos. Trans. R. Soc. London A **251**, 113 (1958).

[12] D. T. Pierce, R. J. Celotta, G.-C. Wang, W. N. Unertl, A. Galejs, C. E. Kuyatt, and S. R. Mielczarek, Rev. Sci. Instrum. **51**, 478 (1980).

[13] J. J. McClelland M. H. Kelley, Phys. Rev. A **31**, 3704 (1985).

[14] L. A. Hodge, T. J. Moravec, F. B. Dunning, and G. K. Walters, Rev. Sci. Instrum. **50**, 271 (1979).

[15] J. J. McClelland, M. R. Scheinfein, and D. T. Pierce, Rev. Sci. Instrum. **60**, 683 (1989).

[16] P. R. Bevington, *Data Reduction and Error Analysis for the Physical Sciences* (McGraw-Hill, New York, 1969).

[17] H. W. Hermann, I. V. Hertel, and M. H. Kelley, J. Phys. B **13**, 3465 (1980).

[18] D. L. Moores and D. W. Norcross, J. Phys. B **5**, 1482 (1972).

[19] A. R. Johnston, Ph.D. thesis, University of Nebraska, 1983.

[20] J. Mitroy, I. E. McCarthy, and A. T. Stelbovics, J. Phys. B **20**, 4827 (1987).